

Perceptually-Based Single-Image Depth Super-Resolution

Oleg Voinov¹, Alexey Artemov¹, Vage Egiazarian¹, Alexander Notchenko¹,
 Gleb Bobrovskikh^{1,2}, Denis Zorin^{3,1}, Evgeny Burnaev¹

¹Skolkovo Institute of Science and Technology, ²Higher School of Economics,
³New York University

{oleg.voinov, a.artemov, vage.egiazarian, alexandr.notchenko}@skoltech.ru,
 bobrovskihg@gmail.com, dzorin@cs.nyu.edu, e.burnaev@skoltech.ru

Abstract

RGBD images, combining high-resolution color and lower-resolution depth from various types of depth sensors, are increasingly common. One can significantly improve the resolution of depth images by taking advantage of color information; deep learning methods make combining color and depth information particularly easy. However, fusing these two sources of data may lead to a variety of artifacts. If depth maps are used to reconstruct 3D shapes, e.g., for virtual reality applications, the visual quality of upsampled images is particularly important. To achieve high-quality results, visual metric need to be taken into account. The main idea of our approach is to measure the quality of depth map upsampling using renderings of resulting 3D surfaces. We demonstrate that a simple visual appearance-based loss, when used with either a trained CNN or simply a deep prior, yields significantly improved 3D shapes, as measured by a number of existing perceptual metrics. We compare this approach with a number of existing optimization and learning-based techniques.

1. Introduction

RGB-D images are increasingly common as sensor technology becomes more widely available and affordable. These images can be used to reconstruct the 3D shapes of objects as well as their surface properties. The better the quality of the depth component, the more reliable the reconstruction is.

Unfortunately, for most methods of depth information acquisition the resolution and quality of the depth component is significantly inferior to the quality of the RGB components. As there is a high correlation between geometric features of the color image and the depth image (e.g., object edges), it is natural to use the color image in the process of improving resolution of the depth image. While model-based methods able to combine color and depth modalities do exist, neural networks are a natural fit for this problem

as they can easily fuse heterogeneous information.

A critical aspect of any upsampling method is the measure of quality (loss function) it optimizes, whether the method is data-driven or not. While the choice is in general application-dependent, many problems share similar criteria for the choice of a quality measure. If the application requires reconstruction of 3D geometry visible to the user (e.g., acquisition of realistic 3D scenes for virtual reality and computer graphics applications), *visual* quality of the result is of particular importance.

Most existing research on depth map super-resolution is dominated by the use of RMSE and its variants for measuring the quality of the resulting upsampled depth image. It is widely recognized that commonly used RMS difference of color image data is not well correlated with perceptual image differences (see [40]). Images (e.g., an image and its blurred version) can be quite close in per-pixel difference metric while differing significantly from perceptual point of view (e.g., more than the same image with all colors changed which may be quite distant in per-pixel difference norm). A variety of perceptually-based measures were proposed for image comparison.

In this paper, we demonstrate that RMSE is also *inadequate* to measure the quality of the resulting 3D surface when used with depth maps. We further demonstrate that by choosing a suitable loss function the perceived quality of the depth map upsampling can be significantly improved. We consider two upsampling methods based on neural nets, integrating perceptually motivated metrics as loss functions. The first is based on a state-of-the-art neural network architecture and requires training, but can be applied efficiently during inference. The second approach is based on deep image priors, a remarkable observation [39], that the structure of the network itself, without any specialized training, may be used for optimization, resulting in a zero-shot upsampling method.

Our choice of the perceptually-based loss function in either case is based on comparison of several commonly used measures of visual similarity. We demonstrate that our choice of the loss, trading complexity vs. strength (*i.e.*, how

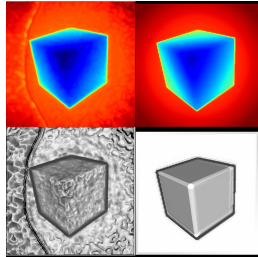


Figure 1: Results of upsampling using RMSE and related BadPix metrics can be visually poor. The top row shows the depth maps. The depth map with better upsampling according to RMSE (left) could have severe visual distortions.

restrictive is the measure) results in a significant improvement compared to other whole-image depth image upsampling methods.

We present a comparison of the proposed method using a set of samples selected from four synthetic and real-world datasets commonly used to evaluate depth image super-resolution and a number of visual quality measures.

In summary, our contributions are:

- We demonstrate that RMSE and related measures do not capture visual quality of 3D surface obtained from depth images compared to specialized perceptually-based quality measures.
- We demonstrate that a simple perceptually-motivated metric for depth image comparison can be, on the one hand, easily combined with neural network-based whole-image upsampling techniques, and, on the other hand, is correlated with more complex perceptually based metrics.
- We demonstrate with extensive comparisons, that two methods for depth image upsampling, one based on trained CNN architecture and the other based on the deep image prior, yield high-quality results as measured by a number of perception-based metrics.

The rest of this paper is organized as follows. Section 2 reviews the image-guided single depth image super-resolution problems and literature on the visual metrics. In Section 3, we discuss our choice of the visually-based metrics used for training and evaluation of the depth upsampling methods, and in Section 4 we summarize the methods themselves. Our computational experiments using a variety of datasets are described in Section 5 (the results are included as supplementary material).

2. Related work

2.1. Depth maps and visual metrics

In most papers on depth image/map reconstruction and upsampling, a limited number of simple image comparison

metrics are used. Mean-square error (MSE) and its variations prevail (*e.g.*, [9, 18, 16, 17]). A common closely related alternative is the fraction of pixels exceeding a given threshold in pointwise differences (the BadPix metrics). For images, these measures do not capture important aspects of human perception [40].

In contrast, visual similarity metrics aim to be consistent with human judgment, *e.g.*, in the sense of similarity ordering (which of two images is more similar to ground truth?). Well-established visual metrics include those based on *structural similarity*: SSIM [41], FSIM [48], MSSIM [42]. We discuss FSIM in greater detail in Section 3.

A different metric, operating both as a visual discriminator (*i.e.*, computing the probability of a pair of images to be perceived as different) and computing a measure of visual difference is presented in [29]. It is based on a sophisticated model of low-level visual processing. The authors show it to perform better on two common visual quality databases compared to one of the variants of structural similarity metrics.

Recently, a number of perceptually-based visual metrics produced by neural nets were proposed (see [49] for a detailed overview). Building on deep features learned for, *e.g.*, a classification task, one may opt for a simple metric in the feature space (*e.g.*, L^2 distance), obtaining a perceptually-based measure. Such *neural net-based metrics* were demonstrated to outperform statistical measures such as SSIM across a variety of deep architectures and training objectives. These approaches are in part motivated by modeling of low-level visual processing with neural nets (see, *e.g.*, [45]).

2.2. The depth super-resolution task and related problems

Depth super-resolution is closely related to a number of other tasks performed on depth maps: in particular, denoising, enhancement, inpainting, and densification (see, *e.g.*, [6, 7, 28, 19, 8, 27, 38, 46]), we focus on papers addressing the super-resolution problem directly. More specifically, we review methods for estimation of high-resolution depth image from a single low-resolution depth image and a high-resolution RGB image. A number of works consider pure depth map upsampling (no RGB), *e.g.*, applying edge-guided [5] and novel view synthesis-based approaches [36]. As a rule, however, recent depth sensors are equipped with a high-resolution color camera, making it natural to consider additional RGB data.

Learning-based methods. Among learning-based methods, convolutional neural networks (CNNs) have achieved impressive performance in high-level computer vision tasks and recently have been applied to depth super-resolution [5, 36, 43, 26, 23, 2, 50, 20, 31, 35].

Most of research on single depth map super-resolution using CNNs has been within the RGB-D framework [26, 35, 43, 31], as color information is easy to integrate into typical CNN architectures. A general approach would stack

multiple stages of convolutional layers to extract multi-resolution features and fuse them to predict a target high-resolution depth. Building upon this idea, [31, 35] add subsequent optimization stages to produce sharper results. The method [20] follows a similar approach: it resolves ambiguity in the low-resolution depth map upsampling by adding high-frequency features from high-resolution RGB data. Other approaches to CNN-based image-guided depth super-resolution include linear filtering with CNN-derived kernels [23], deep fusion of time-of-flight depth and stereo images [2], and a method based on generative adversarial networks [50]. However, no attempts have been made to quantify the quality of the resulting upsampled depth map in terms of the corresponding 3D surface reconstructions; instead, the focus has been on quality measures designed for RGB images, applied to depth map directly. In contrast, we focus on metrics tailored to visual surface quality.

Dictionary learning has been extensively investigated for depth super-resolution, with some representative approaches being [11, 12, 25]. However, dictionary learning is typically restricted to small dimensions and as a result to structurally simpler depth maps as opposed to CNN-based methods that leverage layer-wise training to obtain hierarchical data representations.

One strategy commonly adopted to reduce ambiguity in depth image super-resolution is to combine depth data with a different (and complementary) data, and use a method that can take advantage of the additional data. Instances of these are variational approaches using shape-from-shading optimization to improve single-image depth super-resolution [13], or combining reflectance map estimation with multiple-image depth super-resolution [30]. While showing impressive results in many instances, these methods suffer from the false guidance when the RGB data contains high-frequency details. These methods typically require prior segmentation of foreground objects, depending heavily on the quality of such a segmentation. Additionally, [13] implies that the shape reflectance follows the Potts prior, an assumption often violated in practice. In contrast, our learning-based method makes no assumptions on the reflectance prior. Another strategy to tackle ambiguities in super-resolution is to design sophisticated regularizers to balance the data-fidelity terms against a structural image prior [14, 22, 47]. In contrast to such approaches, which require custom hand-crafted regularized objectives and optimization procedures, the trainable form of our method is standard (*i.e.*, gradient-based optimization of a CNN).

A less common, but promising strategy is to leverage multiple frames of RGB-D video for depth estimation [37]. While we do not consider this setting in our work, we expect that the main elements of the approach we propose also apply in this setting. Yet another approach is to choose a carefully-designed model such as [51] featuring a sophisticated metric defined in a space of minimum spanning trees and including an explicit edge inconsistency model. Compared to our approaches, such models require manual tuning



Figure 2: Renderings of surface used in our evaluation of the perceptually-based metrics.

of multiple hyperparameters.

3. Metrics

To measure the difference between depth images, we consider several metrics distinct from MSE used in most previous works. Our overall approach is to reduce the comparison of depth images to comparison of regular images generated from these depth fields, using various types of standard and perception-based metrics.

From depth maps to images. To approximate the appearance of a 3D model, we use simple diffuse lighting, with directional light sources having light source directions e_i . We do not take visibility into account. We use a camera corresponding to the acquisition point of view. For this simple model, the intensity I_i at a point (x, y) of the depth map is proportional to $e_i \cdot n(x, y)$, where $n(x, y)$ is the value of 3D surface normals that get projected to point (x, y) on the image. If we pick three orthogonal light directions e_1, e_3, e_3 and concatenate the result, we obtain three components of the normal vector in the coordinate system defined by e_i , see Figure 2. Images for any other lighting direction can be obtained as linear combinations of these three images.

This suggests that the *normal image* for the depth map can be viewed as a proxy for the space of possible images generated from the 3D geometry specified by this depth map in this simple model. The normal for a depth map is estimated using standard finite differences.

Low-level error metrics. The simplest difference between depth maps d_1 and d_2 based on visual difference is computed simply as either MSE or absolute value error between the normal images:

$$\mathcal{E}_{\text{RMSE}}(d_1, d_2) = \sqrt{\frac{1}{N} \sum_{i,j} \|n_{ij}^1 - n_{ij}^2\|_2^2},$$

$$\mathcal{E}_{\text{ABS}}(d_1, d_2) = \frac{1}{N} \sum_{i,j} \|n_{ij}^1 - n_{ij}^2\|_1.$$

There are a few closely related metrics, in particular, threshold-based ones, such as BadPix [18]. In our experiments we use another surface-aware error metric, closely related to $\mathcal{E}_{\text{RMSE}}$, which leads to faster convergence:

$$\mathcal{E}_{\text{SURF}}(d_1, d_2) = 1 - (\mathbf{n}^1 \cdot \mathbf{n}^2)^2.$$

Another set of measures introduced in [18] are heuristic measures of various aspects of surface perception: foreground flattening/thinning, fuzziness, bumpiness, etc. Most of them require a very specific segmentation of the image: detection of flat areas and depth discontinuities, which is difficult to do in general case, even for noise-free ground-truth images.

Perceptually-based metrics. We use two most common perceptually-based types of metrics: a statistics-based SSIM, and several metrics based on measuring RMS distances between features in a trained neural net.

SSIM [47]. SSIM (structural similarity index measure) is a widely used metric that aims to take into account changes in local structure of an image, captured by a number of statistical quantities computed on a small window around each pixel. A per-pixel SSIM index is computed, and the mean of per-pixel indices yields a global metric. For each pixel, 3 terms (the luminance term ℓ , the contrast term c and the structural term s , each normalized to be bounded by 1) are multiplied. These terms are computed from the local means μ_x, μ_y , standard deviations σ_x, σ_y and cross-covariance σ_{xy} of corresponding local windows in two images x and y ,

$$l(x, y) = \frac{2\mu_x\mu_y}{\mu_x^2 + \mu_y^2}, \quad c(x, y) = \frac{2\sigma_x\sigma_y}{\sigma_x^2 + \sigma_y^2}, \quad s(x, y) = \frac{\sigma_{xy}\sigma_y}{\sigma_x\sigma_y}$$

with small (relative to range) constants added to each numerator and denominator to avoid undefined behavior for zero means or standard deviations. The luminance and contrast differences are captured by comparing means and standard deviations, and structure similarity is measured by correlation of normalized values in the neighborhood. DSSIM is a rescaling of SSIM computed as $(1 - SSIM)/2$.

Neural net-based metrics. The overall underlying idea of all of these metrics is to compute an L^2 distance between features extracted from a neural network. Specifically, features $\mathbf{x}_\ell, \ell = 1 \dots L$, are extracted from L layers of the network (with different L for each network type). If ℓ -th layer feature is of dimension $H_\ell \times W_\ell \times C_\ell$, where H_ℓ and W_ℓ are spatial dimensions and C_ℓ is the number of channels, then, in the simplest case, the error is computed as

$$\mathcal{E}_{\text{NN}} = \sum_{\ell} \frac{1}{H_\ell W_\ell} \sum_{h,w} \|\hat{\mathbf{x}}_{hw}^{\ell,1} - \hat{\mathbf{x}}_{hw}^{\ell,2}\|_2^2,$$

where $\hat{\mathbf{x}}_{hw}^{\ell}$ denotes the unit normalization of feature vectors along the channel direction. We use [49] choice of networks: Alexnet [24] with, VGG [33] (5 layers are used from both), and SqueezeNet [21] (the first layer is used).

4. Methods

We consider the question whether RMSE provides a good measure of the visual quality of the results produced by existing methods, many of which use RMSE as a loss function, and whether an alternative loss function can do better. Our approach to evaluation is to evaluate a set of

methods in a uniform manner irrespective of the architecture, assessing the visual quality of the resulting 3D surfaces with several perceptual metrics. We have considered a broad range of metrics and identified a representative set (other metric, e.g., neural network-based, are typically correlated with the chosen metrics).

We selected five depth-map upsampling methods with distinct underlying principles: recent CNN-based learnable methods [31, 20, 28, 46, 39], optimization-based [13], and filtering-based approaches [44]. Some of the methods we have included were developed for slightly different tasks but can be easily adapted for super-resolution (which we did). The pure super-resolution methods we include are [31, 20, 13, 44]. Other methods were designed for denoising [46, 12] and densification of sparsely sampled depth images [28]. [39] describes a method for super-resolution of photos, but easily generalizes to depth maps. In this section, we briefly summarize these methods and present two methods based on our approach.

Evaluated methods. *Deep multi-scale guided networks* [20] is a carefully-designed and state-of-the-art deep learning architecture, using different strategies to upsample different spectral components of low-resolution depth map (e.g., high-frequency vs. low-frequency components).

Deep primal-dual networks [31]. Standing out of the typical mostly empirical approaches, the state-of-the-art PDN model features two stages: the first is composed of fully-convolutional layers that produce a rough super-resolved depth, and the second solves an unrolled variational optimization problem that estimates sharp and noise-free results.

Depth super-resolution from shading [13] is a state-of-the-art method relying on a shape-from-shading functional as a part of the process. The method bases on an insight that high-frequency information necessary to achieve depth super-resolution which preserves details could be provided by the photometric data.

Edge-guided depth super-resolution [44] is a depth-only MRF-based super-resolution approach combining depth upsampling with high resolution smooth edge prediction problem.

Deep image prior [39] is a zero-shot image super-resolution algorithm, based on a remarkable observation that the structure of the network itself, without any specialized training, may be used for optimization. We note that this model is mask/hole-agnostic and allows for simultaneous super-resolution & inpainting without any modifications.

All methods (except for [44]) use high-resolution RGB guidance image as additional input. However, no method was evaluated from the point of view of visual quality of the resulting surface.

Our modified methods. To demonstrate the importance of using visually-based loss function, we train a state-of-the-art CNN architecture MSG-Net [20] for upsampling only task and a zero-shot Deep Image Prior model [39] for joint upsampling and hole-filling task. Our visually-based loss

function is the weighted sum of two terms – Laplacian pyramid loss $\mathcal{E}_{\text{LAP}}(d, d^{(\text{HR})})$, see [3], and squared normal deviation $\mathcal{E}_{\text{SURF}}(d, d^{(\text{HR})})$:

$$\hat{d}_*^{(\text{HR})} = \arg \min_{d^{(\text{HR})}} \mathcal{E}_{\text{LAP}}(d, d^{(\text{HR})}) + w \cdot \mathcal{E}_{\text{SURF}}(d, d^{(\text{HR})}). \quad (1)$$

The integration of this loss into both methods is straightforward, but has a dramatic impact on the results.

5. Experiments

In this section, we describe a series of computational experiments to characterize the performance of several methods for super-resolution with respect to visual quality metric.

We start with an experiment for visual surface quality evaluation based on the results produced by a variety of techniques and demonstrate the limitations of RMSE as a visual quality measure. Our second set of experiments shows the advantages of using a visually-based loss for the modified methods. We further investigate a combined hole-filling/super-resolution method in terms of improvement of visual quality of the surface, using the same loss.

5.1. Datasets

We have selected a representative and diverse set of depth images and registered RGB images from four datasets most commonly employed in literature on depth super-resolution [15, 34, 10, 32]. By creating our *SimGeo* dataset and extracting subsets of images from these datasets, we end up with eight evaluation subsets (see the table in supplementary materials for a summary of our evaluation set).

The *SimGeo* dataset has been created using Blender¹ and consists of simple geometric shapes without textures as well as with lower- and higher-detailed textures (aimed to act as high-frequency and low-frequency intensity components). Our goal when using *SimGeo* dataset is to benchmark against a relatively simple set of noise-free depth images, possibly revealing false texture transfer for RGB-guided upsampling methods.

ICL-NUIM [15] is a photo-realistic synthetic dataset obtained using advanced rendering techniques, offering ground truth data for quantitative evaluation of the quality of the final depth-based surface reconstruction. Two different scenes (the living room and the office room scene) are provided. The dataset offers realistic input images along with synthetic ground truth, free from any possible acquisition noise.

A widely used dataset Middlebury 2014 [32] consists of complex real-world scenes captured by an industrial structured light system, with accompanying stereo images. We extract two subsets from this dataset, which we refer to as *Simple* and *Complex*, with *Complex* dataset consisting

of images having significantly finer detailed surfaces compared to *Simple*. Middlebury datasets are a standard benchmark in depth upsampling methods. Due to the careful measurement with precise ground truth, they provide the best available real-world training and testing data.

5.2. The evaluation setup

As discussed in Section 3, for measuring the visual quality we render the surface, corresponding to super-resolved range-image, lit with directional parallel light source from different locations: behind the camera, straight in the viewing direction, upward, downward-left, and downward-right (c.f. Figure 2). In this section we only demonstrate $\times 4$ upsampling results, with renders for $\times 2$ and $\times 8$ upsampling factors provided in the supplementary material.

5.3. Is RMSE correlated with the perceived quality of the 3D surface?

Our first experimental evaluation demonstrates that RMSE-related metrics are not well-correlated with visual surface quality. We run all methods (see section 4) to compute estimates $\hat{d}_{ij}^{(\text{HR})}$ (i indexes methods and j indexes sample depth maps) of high-resolution depth maps given their low-resolution counterparts and corresponding high-resolution RGB images (where applicable). We use the box downsampling to compute the low-resolution depth maps where it is necessary. Using the metrics discussed above (see section 3), we compute distances $e_{ijk} = \mathcal{E}_k(d^{(\text{HR})}, \hat{d}_{ij}^{(\text{HR})})$ (where k indexes metrics). We present a visualization of the correlation between RMSE and visual metrics, as well as correlation between several visual metrics, in Fig. 3. Each point in the plot corresponds to a test image. Note that our visually-based SURF metric correlate with the perceptual losses significantly better than RMSE, although somewhat worse than SSIM correlates with LPIPS. In Fig. 4 we present a subset of the qualitative results and refer to supplementary material for more visualizations.

5.4. Super-resolution results using a visually-based metric proxy

In the following experiment we evaluate our novel visually-based loss function (1). We train MSG-Net on patches, collected from both real-world Middlebury and synthetic MPI Sintel [4] datasets.

Both the qualitative (Fig. 4) and quantitative (Table 1) evaluation according to the perceptual metrics suggest that using visually-based loss function for training leads to significant improvement of visual surface quality. Note that our loss-function not only improves the visual quality of the surface, but also helps to super-resolve fine details, see Fig. 6.

¹Available from <http://www.blender.org/>

Sphere and cylinder $\times 4$					Lucy $\times 4$			
Method	RMSE	SURF	DSSIM	LPIPS	RMSE	SURF	DSSIM	LPIPS
Bicubic	0.057	0.067	0.094	0.312	0.072	0.137	0.176	0.391
SRFS	0.059	0.088	0.215	0.643	0.082	0.297	0.405	0.777
PDN	0.157	0.052	0.130	0.338	0.173	0.143	0.261	0.435
Edge-Guided	0.056	0.032	0.118	0.434	0.069	0.102	0.222	0.497
MSG	0.040	0.063	0.143	0.480	0.054	0.135	0.224	0.482
DIP-MSE	0.049	0.149	0.427	0.909	0.053	0.249	0.413	0.608
MSG-SURF	0.100	0.022	0.038	0.172	0.074	0.056	0.102	0.250
DIP-SURF	0.035	0.037	0.104	0.501	0.044	0.099	0.209	0.435
Livingroom $\times 4$					Recycle $\times 4$			
Method	RMSE	SURF	DSSIM	LPIPS	RMSE	SURF	DSSIM	LPIPS
Bicubic	0.028	0.072	0.211	0.536	0.0210	0.1309	0.3690	0.5623
SRFS	0.039	0.188	0.353	0.608	0.0471	0.2866	0.4056	0.6821
PDN	0.151	0.100	0.256	0.685	0.0912	0.1775	0.3713	0.5941
Edge-Guided	0.036	0.094	0.251	0.735	—	—	—	—
MSG	0.021	0.078	0.247	0.466	0.0974	0.3019	0.4178	0.6752
DIP-MSE	0.030	0.257	0.401	0.632	0.0291	0.3660	0.4664	0.6271
MSG-SURF	0.068	0.039	0.176	0.526	0.0522	0.1526	0.3703	0.5864
DIP-SURF	0.022	0.075	0.283	0.380	0.0204	0.1504	0.3865	0.4993

Table 1: Quantitative comparison. Lower values are better for all metrics; RMSE is in meters.

5.5. Super-resolution and inpainting results using a zero-shot architecture

We observe that due to missing values occurring in the input low-resolution depth maps certain methods (e.g., MSG-Net) output large holes in the upsampled result (see the 3rd row of Fig. 4). Using the modified deep image prior method, we demonstrate that usage of visually-based loss function (1) significantly improves visual quality of the produced surface, see Fig. 5 and Fig. 1. Additional results can be found in the supplementary document.

6. Conclusions

As we observed, common methods for color image-guided depth super-resolution optimize RMSE criterion, often combined with a smoothness penalty. However, this does not guarantee perceptually accurate reconstruction of 3D shapes from depth. Using a range of synthetic and real data we have demonstrated that using a visual metric for 3D surfaces constructed from upsampled depth maps to measure their quality results in better reconstructions from perceptual point of view, when combined with neural network-based upsampling methods. Our metric and learning architecture are relatively simple and we expect that further enhancements will be possible with further development of these ideas. In particular, combining these with inpainting methods to eliminate gaps may be promising.

We have focused on the case of single regularly sampled RGBD images, but a lot of geometric data has less regular form. Thus, the future work would be to adapt the developed methodology to the more general sampling of depth maps (e.g., coming from LIDAR imaging) guided by multiple frames of RGB video. In the most general form, our approach can be extended to point clouds, optionally annotated with a collection of RGB images.

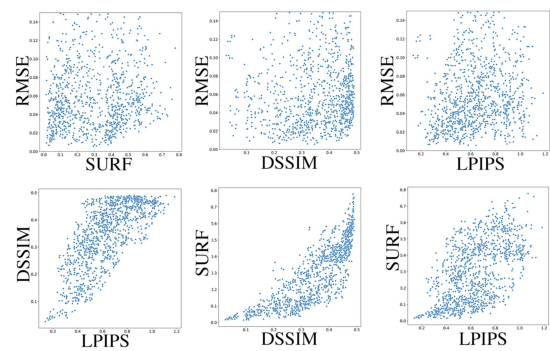


Figure 3: Scatter plots for different metrics used in our evaluation. The top row represent the correlation between visually-based metrics and RMSE. The bottom row represent the correlation between visual metrics.

Acknowledgements

The work was supported by the Ministry of Education and Science of the Russian Federation (Grant no. 14.756.31.0001).

The authors acknowledge the usage of the Skoltech CDISE HPC cluster Zhores for obtaining the results presented in this paper.

Supplementary material

A. RMSE and related metrics and visual surface quality

We present some additional evidence showing that RMSE computed for depth values is not, in general, correlated with visual differences. In Figure 7, we use *depth map* (first column) along with the corresponding *surface renderings* (second column) to display the upsampling results using two CNN-based methods – Deep Image Prior with MSE loss (upper row) and MSG-Net with our SURF loss (lower row). We make two observations. First, the upper image has lower RMS error w.r.t. to the ground truth compared to the lower image, despite being obviously visually inferior, both subjectively and according to the Learned Perceptual Image Patch Similarity (LPIPS) perceptual measure (\mathcal{E}_{NN} in section 3 of the paper). Second, our rendering clearly reveals severe visual distortion, barely visible on the depth map conventionally used to visualize depth processing results.

As suggested by the deviation masks in the third column, higher RMS error for the method with our SURF loss (lower row) is due to the systematic underestimation of depth values in the background. For our target applications, such systematic error is of less importance compared to the visual distortions.

Similarly, in this example, the value of the BadPix metric defined as the fraction of the pixels with absolute deviation larger than a certain threshold t , for various thresholds t is significantly lower (better) for the result corresponding to lower visual quality (Figure 8).

B. Description of the evaluation dataset

In this section, we provide details on our evaluation datasets, summarized in Table 2.

The *SimGeo* dataset (Figures 10, 11 and 12) has been created using Blender² and consists of simple geometric shapes³ without textures as well as with lower- and higher-detailed textures (aimed to act as high-frequency and low-frequency intensity components). Our goal when using *SimGeo* dataset is to benchmark against a relatively simple set of noise-free depth images, possibly revealing false texture transfer for RGB-guided upsampling methods.

²<http://www.blender.org/>

³and also the “Lucy” model from The Stanford 3D Scanning Repository [1]

Dataset	Acquisition method
Our <i>SimGeo</i>	render
ICL-NUIM [15]	render
Middlebury 2014 [32]	
<i>Simple</i>	structured light
<i>Complex</i>	structured light
SUN RGB-D [34]	
<i>KinectV2</i>	time-of-flight
<i>RealSense</i>	structured light
<i>Xtion</i>	structured light
ToFMark [10]	structured light GT & time-of-flight LR

Table 2: Overview of evaluation subsets.

ICL-NUIM [15] (Figure 13) is a photo-realistic synthetic dataset obtained using advanced rendering techniques, offering ground truth data for quantitative evaluation of the quality of the final depth-based surface reconstruction. Two different scenes (the living room and the office room scene) are provided. The dataset offers realistic input images along with synthetic ground truth, free from any possible acquisition noise.

A widely used Middlebury 2014 [32] dataset (Figure 14) consists of complex real-world scenes captured by an industrial structured light system, with accompanying stereo images. We extract two subsets from this dataset, which we refer to as *Simple* and *Complex*, with samples from *Complex* subset having significantly finer surface detail or more complex texture, compared to the samples from *Simple* subset.

SUN RGB-D [34] (Figures 15, 16 and 17) is a dataset containing >10K RGB-D images with dense annotations in both 2D and 3D, for both objects and rooms, captured by four different sensors, including Intel RealSense, Asus Xtion, Kinect v1, and Kinect v2 devices. We select subsets of data corresponding to *RealSense*, *Xtion*, and *Kinect v2* devices, named accordingly.

ToFMark [10] (Figure 18) is a challenging real-world benchmark dataset providing real time-of-flight and intensity camera acquisitions together with an accurate ground truth measurement using a structured light sensor. We include this dataset in our evaluation as we believe it provides one of the most challenging time-of-flight real-world setups available.

C. Details of the evaluation process

In the literature on range-image processing, the term *depth* denotes three different types of range data:

- *disparity* (Middlebury 2014 dataset), commonly de-

noting the difference in image location of a feature within two stereo images;

- *orthogonal depth* (ICL-NUIM and SUN-RGBD datasets and the high resolution scans in the ToFMark dataset), corresponding to the distance from a point in the 3D-space to the image plane;
- *perspective depth* (low-resolution scans in the ToFMark datasets), corresponding to the distance from a point in the 3D-space to the camera.

We do not generally differentiate between these three types of range data and use the term *depth map* to denote any data of this kind. However, in our experiments we use the exact type of depth that a method was designed for. For evaluation of the methods designed for disparity processing, we calculate virtual disparity images with the baseline of 20 cm for the datasets, containing either orthogonal or perspective depth. For measuring the quality of the results and their visualization, the output of each method is converted to perspective depth in meters.

In what follows, we denote high-resolution ground-truth depth-image by $d^{(\text{HR})}$, low-resolution depth-image by $d^{(\text{LR})}$, and super-resolved depth-image by $\hat{d}^{(\text{SR})}$.

We consider the following methods.

Depth super-resolution from shading [13] (*SRfS*). We use the MATLAB implementation of this method shared with us by the authors.

Edge-guided depth super-resolution [44] (*Edge-Guided*). We use the publicly available MATLAB code⁴. We find that the method converges slowly for the samples from Middlebury dataset. For this reason, we only include results obtained within the allowed 3 hours of running time.

Deep primal-dual networks [31] (*PDN*). We use the publicly available LuaTorch implementation⁵.

Learnable dynamic guidance [12] (*Dynamic Guidance*). We use the publicly available MATLAB implementation⁶.

Deep multi-scale guided networks [20] (*MSG, MSG-SURF*). The original model, denoted by *MSG*, is trained using MSE loss on the high-frequency component of the depth-image. For this version, we use the publicly available Caffe implementation and the pretrained models⁷. The *MSG-SURF* version is trained just like the original one, only with our loss with the SURF weight $w = 0.3$ (*MSG* was reimplemented in PyTorch to change the loss).

$$\mathcal{E}_{\text{LAP}}(\hat{d}^{(\text{SR})}, d^{(\text{HR})}) + w \cdot \mathcal{E}_{\text{SURF}}(\hat{d}^{(\text{SR})}, d^{(\text{HR})}). \quad (2)$$

where $\mathcal{E}_{\text{SURF}}(d_1, d_2) = 1 - \frac{1}{N} \sum_{i,j} (n_{1,ij} \cdot n_{2,ij})^2$.

⁴<https://github.com/ClaireXie/edgeGuidedSDSP>

⁵<https://github.com/griegler/primal-dual-networks>

⁶<https://sites.google.com/site/shuhanggu/home>

⁷<https://github.com/twhui/MSG-Net>

Deep image prior [39] (*DIP-MSE, DIP-SURF*). Original Deep Image Prior approach to the super-resolution problem is to solve

$$\hat{d}^{(\text{SR})} = \text{CNN}_{\theta^*}, \quad (3a)$$

$$\theta^* = \arg \min_{\theta} \mathcal{E}_{\text{MSE}}(\mathbf{D}(\text{CNN}_{\theta}), d^{(\text{LR})}), \quad (3b)$$

where d is the output of the used deep neural network parametrised by θ and \mathbf{D} is the downsampling operator. We modify this approach for the problem of guided super-resolution simply by changing the number of output channels produced by the neural network from one to two, with the added intensity channel, so the problem statement becomes

$$\hat{d}^{(\text{SR})} = \text{CNN}_{\theta^*,1}, \quad (4a)$$

$$\theta^* = \arg \min_{\theta} \mathcal{E}_{\text{d}}(\mathbf{D}(\text{CNN}_{\theta,1}), d^{(\text{LR})}) + \quad (4b)$$

$$\mathcal{E}_{\text{I}}(\text{CNN}_{\theta,2}, I^{(\text{HR})}), \quad (4c)$$

where $I^{(\text{HR})}$ is the high-resolution intensity guidance. We use the publicly available PyTorch implementation⁸ and evaluate two versions of this model, denoted by *DIP-MSE* and *DIP-SURF*. For the depth term we use MSE loss and our loss (2) with the SURF weight $w = 0.05$ correspondingly. For the intensity term we use Laplacian pyramid loss \mathcal{E}_{LAP} for both versions of the model.

We briefly mention two more methods we have experimented with, Deep sparse-to-dense regression networks [28], and Deep denoising and refinement networks [46], solving somewhat different but related problems with publicly available code. We found that direct adaptation of these methods to the problem at hand (e.g., replacing the sparse unordered set of samples in [28] with the low-resolution depth map), does not produce results of quality competitive with other methods on any measure.

D. Training results using the structural similarity loss

In the paper we have focused on the simple SURF loss. We did an experiment with the possibility of using a perceptual metric directly, namely DSSIM, instead of our SURF proxy as the loss function. For this purpose, we evaluate the third version of DIP model, *DIP-DSSIM*, for which the depth loss term in (4) is

$$\mathcal{E}_{\text{LAP}}(\mathbf{D}(\text{CNN}_{\theta,1}), d^{(\text{LR})}) + \mathcal{E}_{\text{DSSIM}}(\mathbf{D}(\text{CNN}_{\theta,1}), d^{(\text{LR})}). \quad (5)$$

Counter-intuitively, this version of the model gets lower scores according to DSSIM metric itself (see Figure 9), so we hypothesize that, in its basic form, such loss is more prone to getting stuck in local minima and more difficult to optimize compared to our proxy.

⁸<https://github.com/DmitryUlyanov/deep-image-prior>

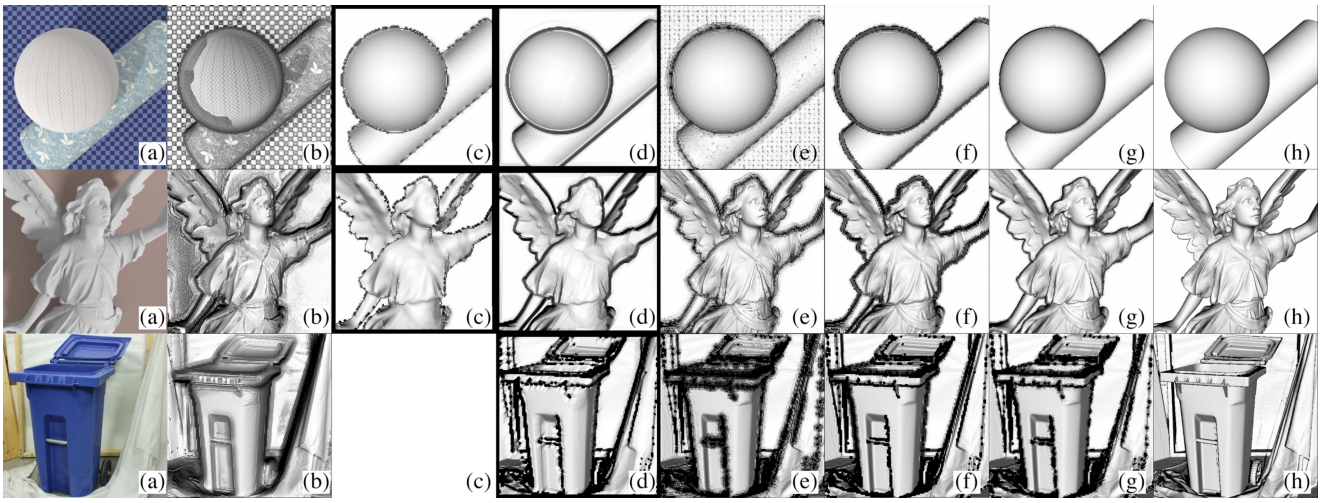


Figure 4: A visual comparison of the results obtained or set of methods, visualized using simple single-source lighting. a) RGB, b) SRfS [13], c) Edge-Guided [44] (the method [44] failed completely on this sample), d) PDN [31], e) MSG [20], f) Bicubic, g) MSG-SURF, h) GT.

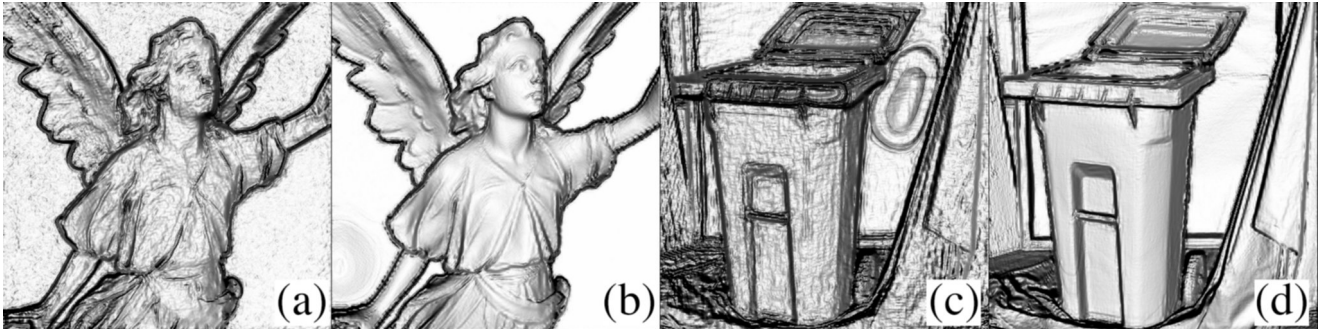


Figure 5: The visual comparison of the results, obtained with [39] using MSE loss – a) and c), and our loss – b) and f).

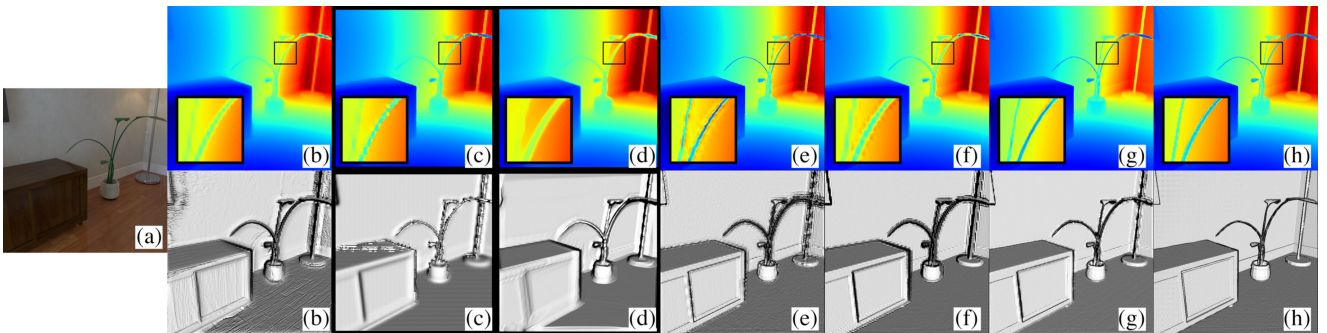


Figure 6: 4x super-resolution for the "Living Room" sample from ICL-NUIM dataset. a) RGB, b) SRfS [13], c) Edge-Guided [44], d) PDN [31], e) MSG [20], f) Bicubic, g) MSG-SURF, h) GT.

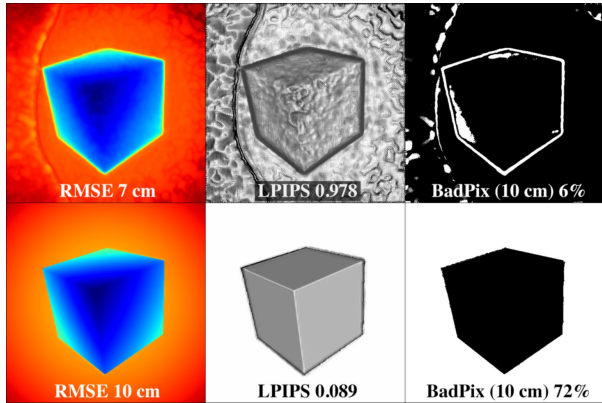


Figure 7: 4x super-resolution with DIP-MSE in the upper row and with MSG-SURF in the lower row. From left to right: super-resolved depth maps, corresponding surface renderings with directional lighting along the viewing direction, and deviation masks (pixels deviating more than 10 cm are colored white). Despite having lower RMS error and less *bad pixels*, the result in the upper row is visually inferior to the result in the lower row, both subjectively and in terms of the LPIPS measure.

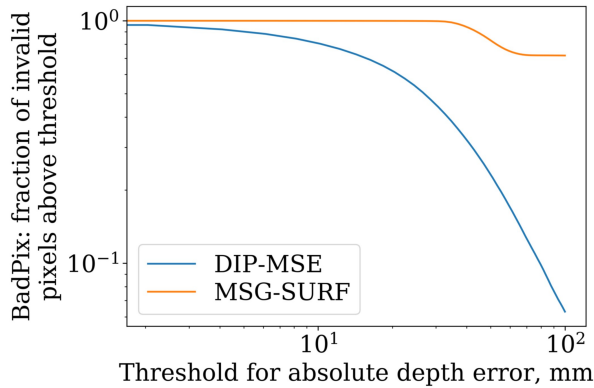


Figure 8: BadPix series for the results depicted in Figure 7.



Figure 9: 4x super-resolution with DIP-SURF on the left and with DIP-DSSIM on the right.

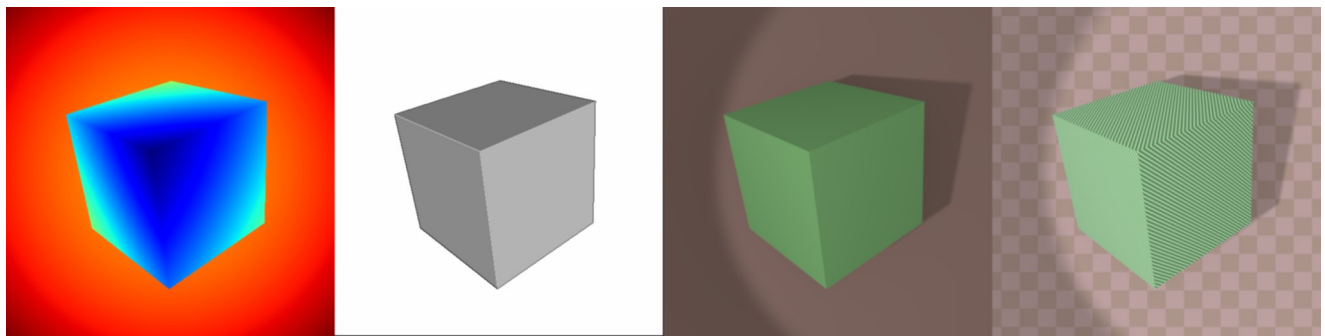


Figure 10: “Cube on plane” sample: depth-image, surface rendering and two versions of RGB image – without and with texture.

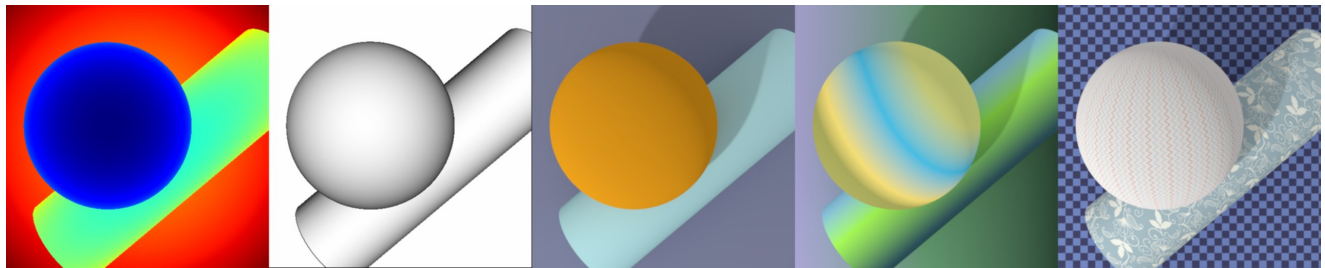


Figure 11: “Sphere and cylinder” sample: depth-image, surface rendering and three versions of RGB image – without, with low-frequency and with high-frequency texture.

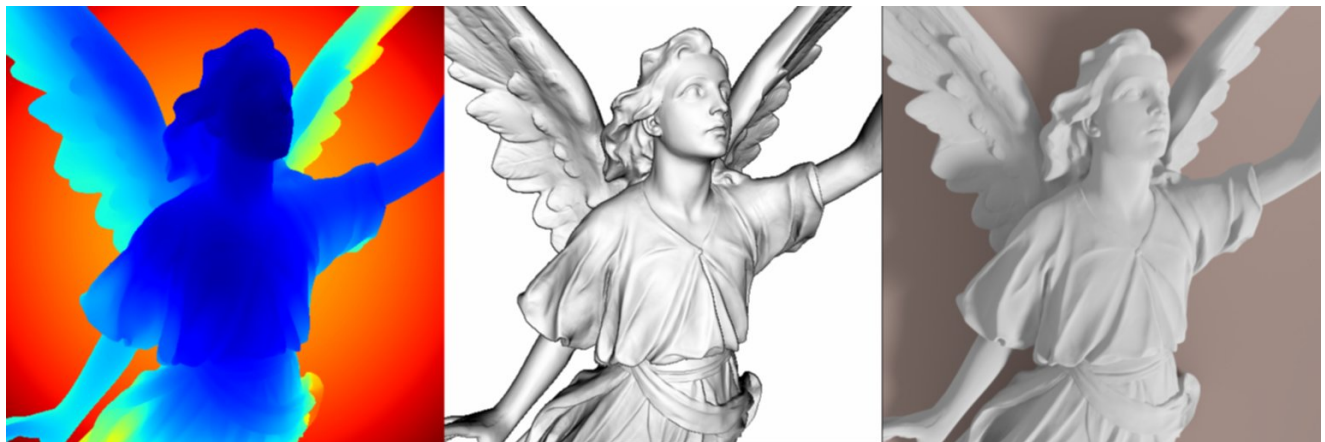


Figure 12: “Lucy” sample: depth-image, surface rendering and RGB image.

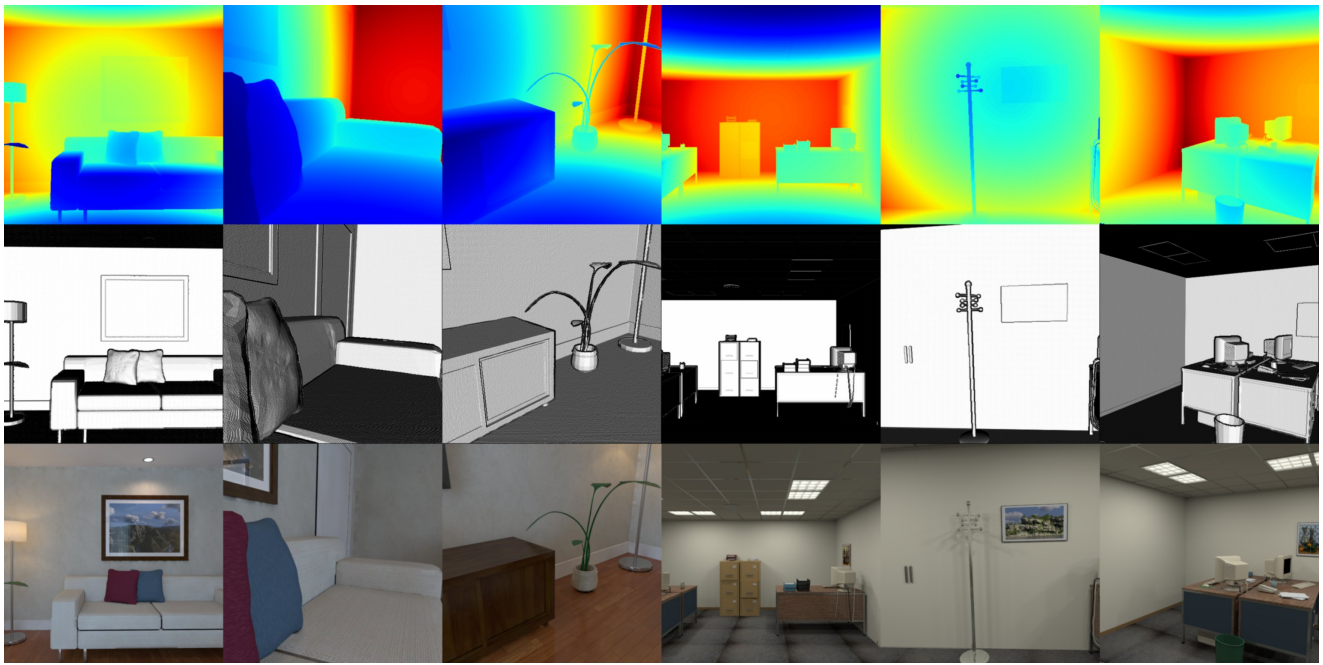


Figure 13: Samples from ICL-NUIM dataset. From top to bottom: depth-image, surface rendering and RGB image.

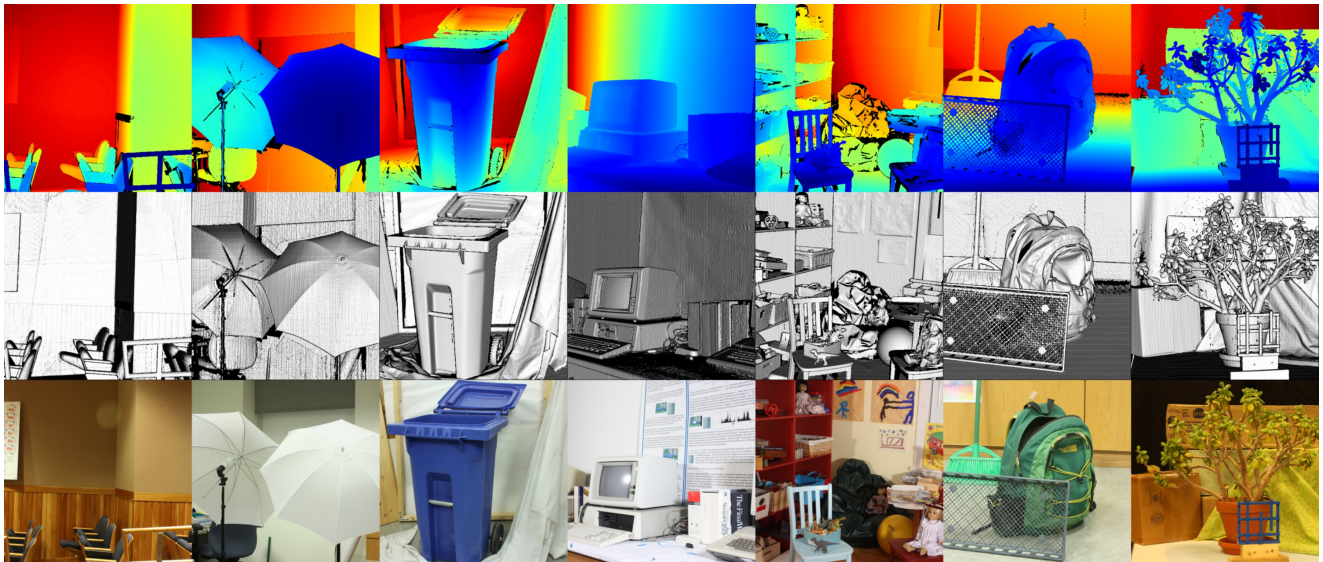


Figure 14: Samples from Middlebury 2014 dataset. From top to bottom: depth-image, surface rendering and RGB image. The first four correspond to the “Simple” subset, and the last three correspond to the “Complex” subset.

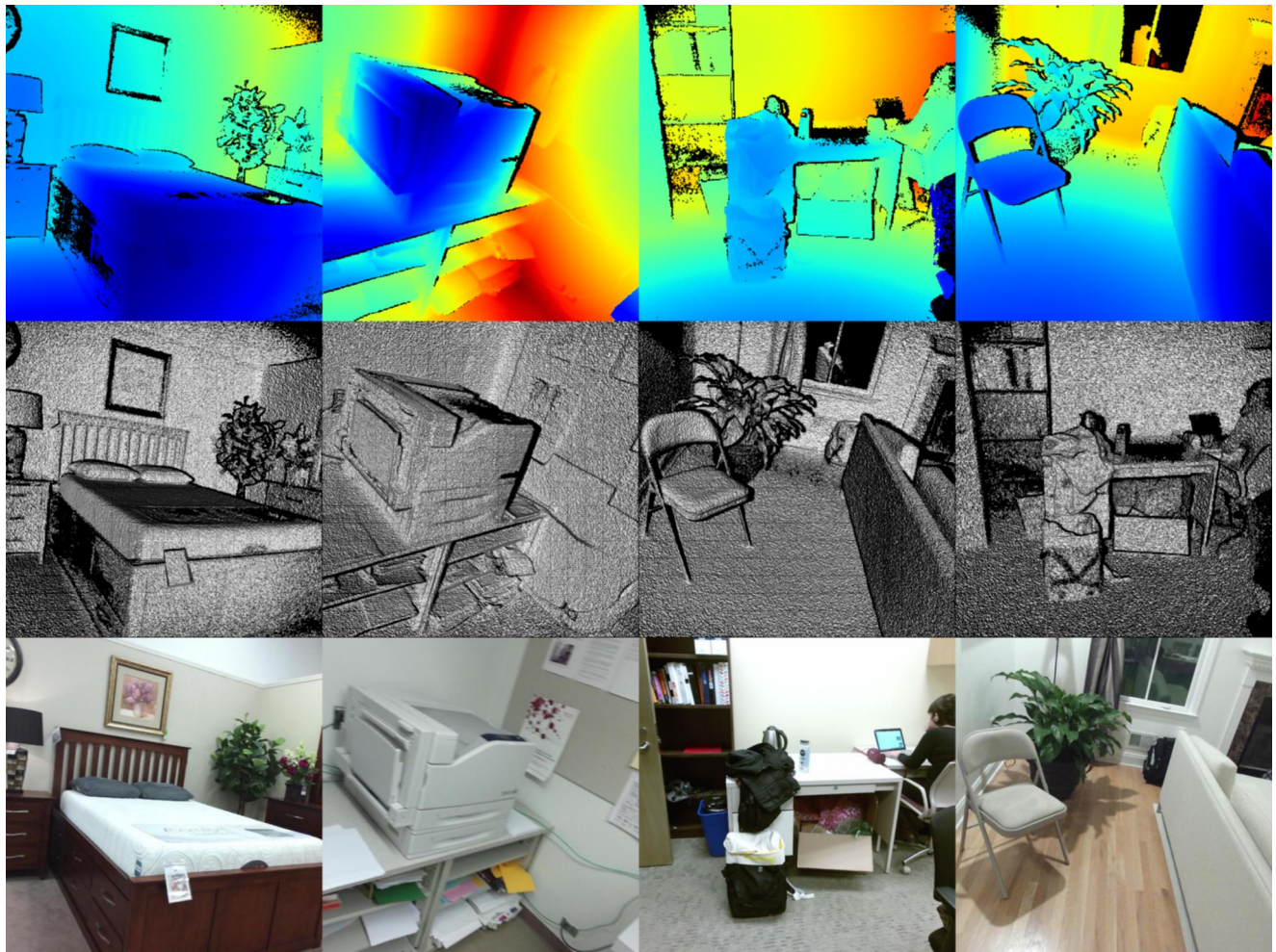


Figure 15: Samples from SUN-RGBD dataset acquired with the Kinect v2 sensor. From top to bottom: depth-image, surface rendering and RGB image.

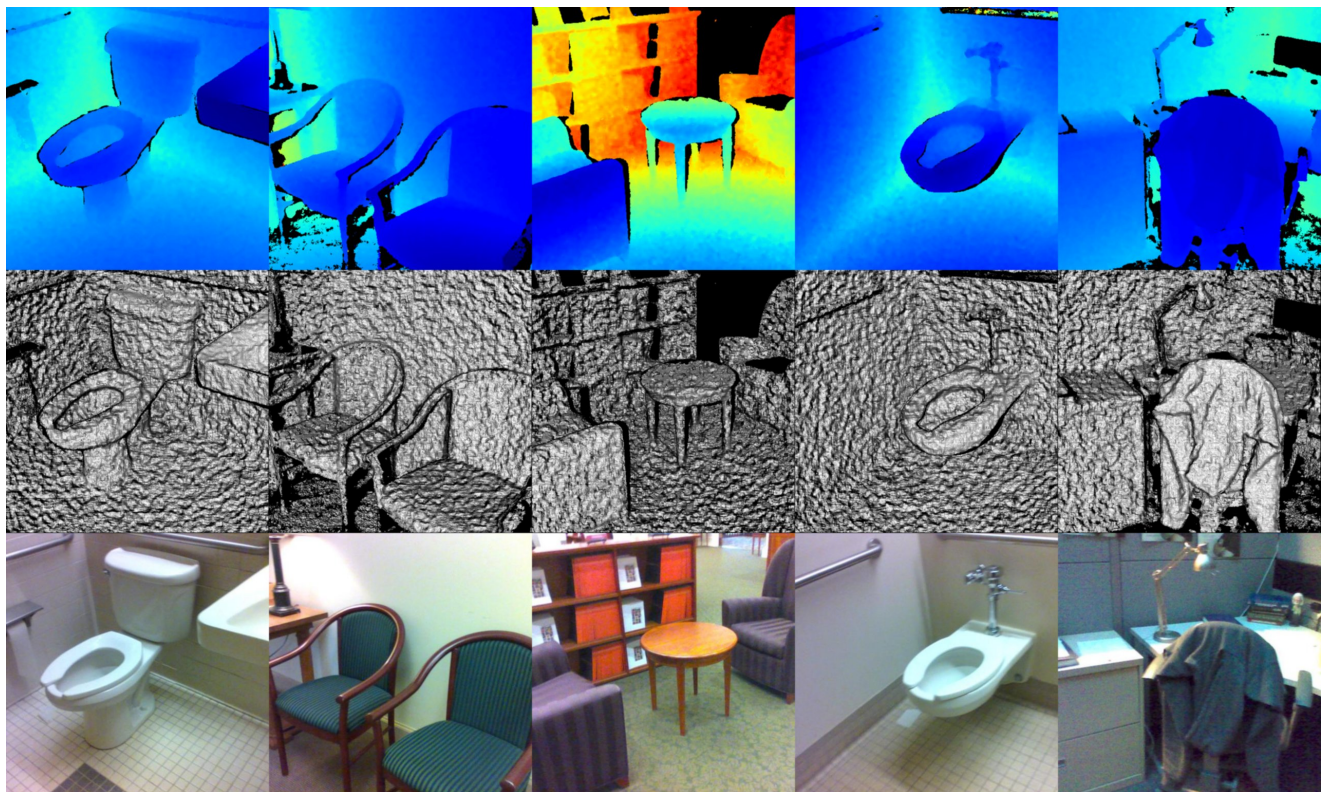


Figure 16: Samples from SUN-RGBD dataset acquired with the Intel RealSense sensor. From top to bottom: depth-image, surface rendering and RGB image.

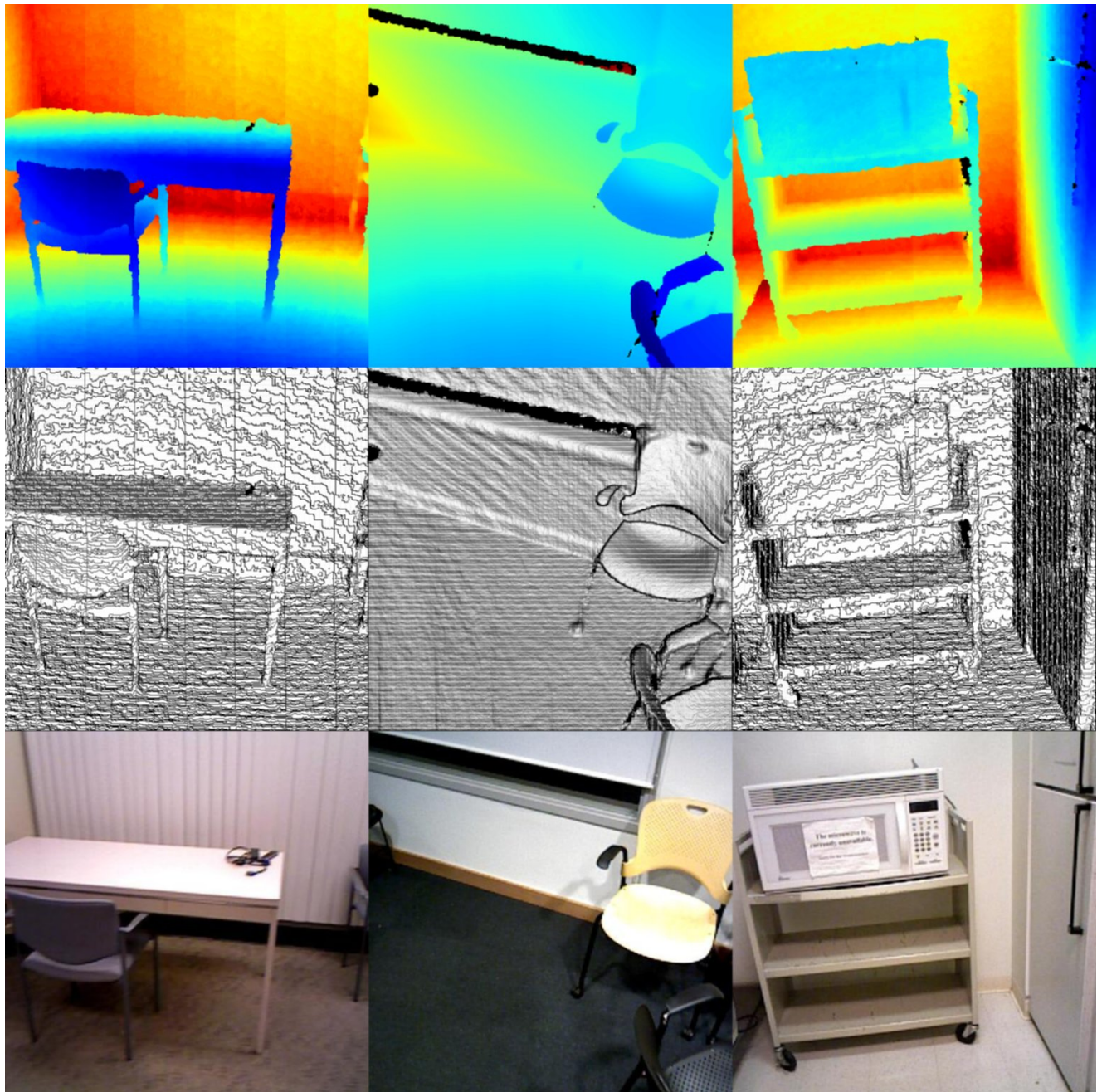


Figure 17: Samples from SUN-RGBD dataset acquired with the ASUS Xtion sensor. From top to bottom: depth-image, surface rendering and RGB image.

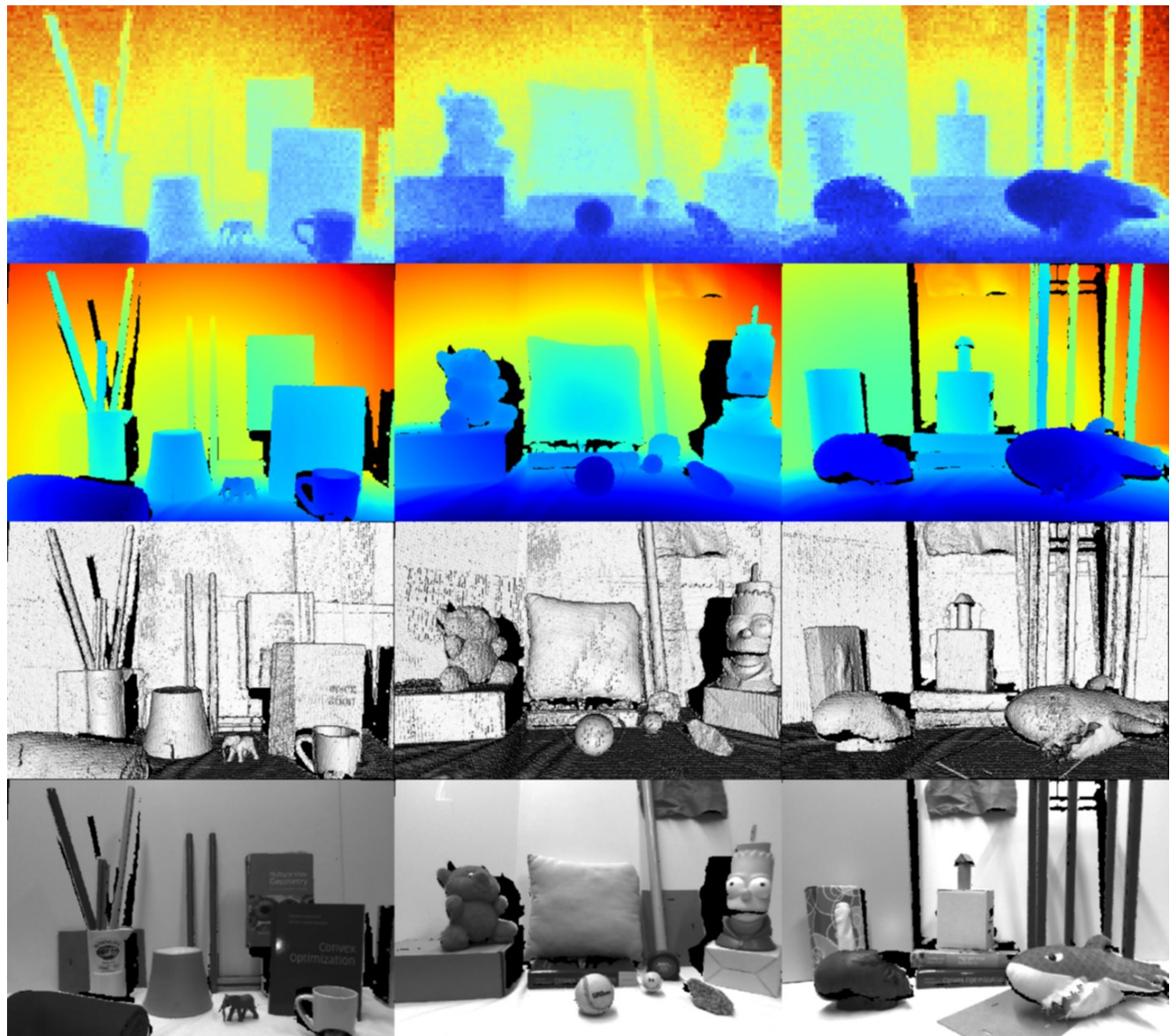


Figure 18: Samples from ToFMark dataset. From top to bottom: low-resolution time-of-flight depth-image, high-resolution structured-light depth-image, surface rendering, corresponding to high-resolution depth-image and RGB image.

References

[1] The stanford 3d scanning repository. <http://graphics.stanford.edu/data/3Dscanrep>. Accessed: 2018-11-18. 7

[2] G. Agresti, L. Minto, G. Marin, and P. Zanuttigh. Deep learning for confidence information in stereo and tof data fusion. In *Proceedings of the IEEE Conference on Computer Vision and Pattern Recognition*, pages 697–705, 2017. 2, 3

[3] P. Bojanowski, A. Joulin, D. Lopez-Pas, and A. Szlam. Optimizing the latent space of generative networks. In J. Dy and A. Krause, editors, *Proceedings of the 35th International Conference on Machine Learning*, volume 80 of *Proceedings of Machine Learning Research*, pages 600–609, Stockholm, Sweden, 10–15 Jul 2018. PMLR. 5

[4] D. J. Butler, J. Wulff, G. B. Stanley, and M. J. Black. A naturalistic open source movie for optical flow evaluation. In A. Fitzgibbon et al. (Eds.), editor, *European Conf. on Computer Vision (ECCV)*, Part IV, LNCS 7577, pages 611–625. Springer-Verlag, Oct. 2012. 5

[5] B. Chen and C. Jung. Single depth image super-resolution using convolutional neural networks. In *2018 IEEE International Conference on Acoustics, Speech and Signal Processing (ICASSP)*, pages 1473–1477. IEEE, 2018. 2

[6] Z. Chen, V. Badrinarayanan, G. Drosdov, and A. Rabovich. Estimating depth from rgb and sparse sensing. *CoRR*, abs/1804.02771, 2018. 2

[7] X. Cheng, P. Wang, and R. Yang. Depth estimation via affinity learned with convolutional spatial propagation network. In *European Conference on Computer Vision*, pages 108–125. Springer, Cham, 2018. 2

[8] N. Chodosh, C. Wang, and S. Lucey. Deep convolutional compressed sensing for lidar depth completion. *arXiv preprint arXiv:1803.08949*, 2018. 2

[9] D. Eigen, C. Puhrsch, and R. Fergus. Depth map prediction from a single image using a multi-scale deep network. In *Advances in neural information processing systems*, pages 2366–2374, 2014. 2

[10] D. Ferstl, C. Reinbacher, R. Ranftl, M. Rüther, and H. Bischof. Image guided depth upsampling using anisotropic total generalized variation. In *Proceedings of the IEEE International Conference on Computer Vision*, pages 993–1000, 2013. 5, 7

[11] D. Ferstl, M. Rüther, and H. Bischof. Variational depth superresolution using example-based edge representations. In *Proceedings of the IEEE International Conference on Computer Vision*, pages 513–521, 2015. 3

[12] S. Gu, W. Zuo, S. Guo, Y. Chen, C. Chen, and L. Zhang. Learning dynamic guidance for depth image enhancement. In *Proceedings of the IEEE Conference on Computer Vision and Pattern Recognition*, pages 3769–3778, 2017. 3, 4, 8

[13] B. Haefner, Y. Quéau, T. Möllenhoff, and D. Cremers. Fight ill-posedness with ill-posedness: Single-shot variational depth super-resolution from shading. In *Proceedings of the IEEE Conference on Computer Vision and Pattern Recognition*, pages 164–174, 2018. 3, 4, 8, 9

[14] B. Ham, M. Cho, and J. Ponce. Robust guided image filtering using nonconvex potentials. *IEEE transactions on pattern analysis and machine intelligence*, 40(1):192–207, 2018. 3

[15] A. Handa, T. Whelan, J. McDonald, and A. Davison. A benchmark for RGB-D visual odometry, 3D reconstruction and SLAM. In *IEEE Intl. Conf. on Robotics and Automation, ICRA*, Hong Kong, China, May 2014. 5, 7

[16] K. Honauer, O. Johannsen, D. Kondermann, and B. Goldluecke. A dataset and evaluation methodology for depth estimation on 4d light fields. In *Asian Conference on Computer Vision*, pages 19–34. Springer, 2016. 2

[17] K. Honauer, O. Johannsen, D. Kondermann, and B. Goldluecke. A dataset and evaluation methodology for depth estimation on 4d light fields. In *Asian Conference on Computer Vision*. Springer, 2016. 2

[18] K. Honauer, L. Maier-Hein, and D. Kondermann. The hci stereo metrics: Geometry-aware performance analysis of stereo algorithms. In *Proceedings of the IEEE International Conference on Computer Vision*, pages 2120–2128, 2015. 2, 3, 4

[19] J. Hua and X. Gong. A normalized convolutional neural network for guided sparse depth upsampling. In *IJCAI*, pages 2283–2290, 2018. 2

[20] T.-W. Hui, C. C. Loy, and X. Tang. Depth map super-resolution by deep multi-scale guidance. In *European Conference on Computer Vision*, pages 353–369. Springer, 2016. 2, 3, 4, 8, 9

[21] F. N. Iandola, S. Han, M. W. Moskewicz, K. Ashraf, W. J. Dally, and K. Keutzer. SqueezeNet: Alexnet-level accuracy with 50x fewer parameters and \downarrow 0.5mb model size. In *The IEEE Conference on Computer Vision and Pattern Recognition (CVPR)*, 2016. 4

[22] Z. Jiang, Y. Hou, H. Yue, J. Yang, and C. Hou. Depth super-resolution from rgb-d pairs with transform and spatial domain regularization. *IEEE Transactions on Image Processing*, 27(5):2587–2602, 2018. 3

[23] B. Kim, J. Ponce, and B. Ham. Deformable Kernel Networks for Joint Image Filtering. working paper or preprint, Oct. 2018. 2, 3

[24] A. Krizhevsky, I. Sutskever, and G. E. Hinton. Imagenet classification with deep convolutional neural networks. In *Advances in neural information processing systems*, pages 1097–1105, 2012. 4

[25] B. Li, Y. Zhou, Y. Zhang, and A. Wang. Depth image super-resolution based on joint sparse coding. *Pattern Recognition Letters*, 2018. 3

[26] Y. Li, J.-B. Huang, N. Ahuja, and M.-H. Yang. Deep joint image filtering. In *European Conference on Computer Vision*, pages 154–169. Springer, 2016. 2

[27] F. Ma, G. V. Cavalheiro, and S. Karaman. Self-supervised sparse-to-dense: Self-supervised depth completion from lidar and monocular camera. *arXiv preprint arXiv:1807.00275*, 2018. 2

[28] F. Mal and S. Karaman. Sparse-to-dense: Depth prediction from sparse depth samples and a single image. In *2018 IEEE International Conference on Robotics and Automation (ICRA)*, pages 1–8. IEEE, 2018. 2, 4, 8

[29] R. Mantiuk, K. J. Kim, A. G. Rempel, and W. Heidrich. Hdr-vdp-2: a calibrated visual metric for visibility and quality predictions in all luminance conditions. In *ACM Transactions on graphics (TOG)*, volume 30, page 40. ACM, 2011. 2

[30] S. Peng, B. Haefner, Y. Queau, and D. Cremers. Depth super-resolution meets uncalibrated photometric stereo. In *Proceedings of the IEEE International Conference on Computer Vision*, pages 2961–2968, 2017. 3

[31] D. Riegler, Gernot aand Ferstl, M. Rüther, and H. Bischof. A deep primal-dual network for guided depth super-resolution. In *British Machine Vision Conference*. The British Machine Vision Association, 2016. 2, 3, 4, 8, 9

[32] D. Scharstein, H. Hirschmüller, Y. Kitajima, G. Krathwohl, N. Nešić, X. Wang, and P. Westling. High-resolution stereo datasets with subpixel-accurate ground truth. In *German Conference on Pattern Recognition*, pages 31–42. Springer, 2014. 5, 7

[33] K. Simonyan and A. Zisserman. Very deep convolutional networks for large-scale image recognition. *CoRR*, abs/1409.1556, 2014. 4

[34] S. Song, S. P. Lichtenberg, and J. Xiao. Sun rgb-d: A rgb-d scene understanding benchmark suite. In *Proceedings of the IEEE conference on computer vision and pattern recognition*, pages 567–576, 2015. 5, 7

[35] X. Song, Y. Dai, and X. Qin. Deep depth super-resolution: Learning depth super-resolution using deep convolutional neural network. In *Asian Conference on Computer Vision*, pages 360–376. Springer, 2016. 2, 3

[36] X. Song, Y. Dai, and X. Qin. Deeply supervised depth map super-resolution as novel view synthesis. *IEEE Transactions on Circuits and Systems for Video Technology*, 2018. 2

[37] A. Tsuchiya, D. Sugimura, and T. Hamamoto. Depth up-sampling by depth prediction. In *2017 IEEE International Conference on Image Processing (ICIP)*, pages 1662–1666, Sept 2017. 3

[38] J. Uhrig, N. Schneider, L. Schneider, U. Franke, T. Brox, and A. Geiger. Sparsity invariant cnns. In *IEEE International Conference on 3D Vision (3DV)*, 2017. 2

[39] D. Ulyanov, A. Vedaldi, and V. Lempitsky. Deep image prior. In *The IEEE Conference on Computer Vision and Pattern Recognition (CVPR)*, June 2018. 1, 4, 8, 9

[40] Z. Wang and A. C. Bovik. Mean squared error: Love it or leave it? a new look at signal fidelity measures. *IEEE signal processing magazine*, 26(1):98–117, 2009. 1, 2

[41] Z. Wang, A. C. Bovik, H. R. Sheikh, and E. P. Simoncelli. Image quality assessment: from error visibility to structural similarity. *IEEE transactions on image processing*, 13(4):600–612, 2004. 2, 4

[42] Z. Wang, E. P. Simoncelli, and A. C. Bovik. Multiscale structural similarity for image quality assessment. In *The Thirty-Seventh Asilomar Conference on Signals, Systems & Computers, 2003*, volume 2, pages 1398–1402. IEEE, 2003. 2

[43] Y. Xiao, X. Cao, X. Zhu, R. Yang, and Y. Zheng. Joint convolutional neural pyramid for depth map super-resolution. *arXiv preprint arXiv:1801.00968*, 2018. 2

[44] J. Xie, R. S. Feris, and M.-T. Sun. Edge-guided single depth image super resolution. *IEEE Transactions on Image Processing*, 25(1):428–438, 2016. 4, 8, 9

[45] D. L. Yamins and J. J. DiCarlo. Using goal-driven deep learning models to understand sensory cortex. *Nature neuroscience*, 19(3):356, 2016. 2

[46] S. Yan, C. Wu, L. Wang, F. Xu, L. An, K. Guo, and Y. Liu. Ddrnet: Depth map denoising and refinement for consumer depth cameras using cascaded cnns. In *Proceedings of the European Conference on Computer Vision (ECCV)*, pages 151–167, 2018. 2, 4, 8

[47] J. Yang, X. Ye, K. Li, C. Hou, and Y. Wang. Color-guided depth recovery from rgb-d data using an adaptive autoregressive model. *IEEE transactions on image processing*, 23(8):3443–3458, 2014. 3

[48] L. Zhang, L. Zhang, X. Mou, D. Zhang, et al. Fsim: a feature similarity index for image quality assessment. *IEEE transactions on Image Processing*, 20(8):2378–2386, 2011. 2

[49] R. Zhang, P. Isola, A. A. Efros, E. Shechtman, and O. Wang. The unreasonable effectiveness of deep features as a perceptual metric. In *The IEEE Conference on Computer Vision and Pattern Recognition (CVPR)*, June 2018. 2, 4

[50] L. Zhao, H. Bai, J. Liang, B. Zeng, A. Wang, and Y. Zhao. Simultaneously color-depth super-resolution with conditional generative adversarial network. *arXiv preprint arXiv:1708.09105*, 2017. 2, 3

[51] Y. Zuo, Q. Wu, J. Zhang, and P. An. Minimum spanning forest with embedded edge inconsistency measurement model for guided depth map enhancement. *IEEE Transactions on Image Processing*, 27(8):4145–4159, 2018. 3